ISSN (Print) 1226-1750
ISSN (Online) 2233-6656
Journal of Magnetics 26(4), 363-377 (2021) https://doi.org/10.4283/JMAG.2021.26.4.363

Significance of Buongiorno Model and Arrhenius Pre-exponential Factor Law to Entropy Optimized Darcy Forchheimer Hybrid Nanoparticle (Al_2O_3, Cu) Flow Over Thin Needle

S. Shaw[1], M. Ijaz Khan[2]*, M. K. Nayak[3], J. K. Madhukesh[4], R. S. Varun Kumar[4], Shahid Farooq[2], and M. Y. Malik[5]

[1]*Department of Mathematics and Statistical Sciences, Botswana International University of Science and Technology, Private Bag 16, Palapye, Botswana*
[2]*Department of Mathematics and Statistics, Riphah International University I-14, Islamabad 44000, Pakistan*
[3]*Department of Mechanical Engineering, FET, ITER, Siksha 'O' Anusandhan Deemed to be University, Bhubaneswar-751030, India*
[4]*Department of Mathematics, Davangere University, Davangere, Karnataka, India*
[5]*Department of Mathematics, College of Sciences, King Khalid University, Abha 61413, Saudi Arabia*

(Received 17 August 2021, Received in final form 7 October 2021, Accepted 26 October 2021)

In the fields of engineering, industry, and biology, thin needles serve a critical role. The thermocouple hot wire anemometer for wind speed monitoring, microscale heat extraction cooling systems, and electronic microstructure outfitting are only a few of the needle's key applications. In view of these applications the present investigation is carried out to study the Casson hybrid nanofluid flow for the entropy creation and the pre-exponential factor law in Darcy Forchheimer medium on the thin needle. The set of governing equations describing the flow problem will be converted to a system of ordinary differential equations with suitable similarity variables. The numerical solutions are obtained by the aid of mathematical computing software by applying the Runge Kutta Fehlberg 45 method with shooting scheme. The numerical results for various parameters are produced, and an entropy analysis is performed. Axial velocity falls as the porosity and Darcy parameters are increased. The thermal performance improves as the needle size and Brinkman number increase. The concentration profile is improved by thermophoresis, Brinkman number, and activation energy parameter. The entropy generation and surface drag force will increase as the porosity parameters are increased, while the Bejan number will decrease.

Keywords : casson hybrid nanofluid, thin needle, darcy-forchheimer flow, buongiorno model, thermal radiation

Nomenclature

(u, v) : Velocity components in the axial and radial directions (ms^{-1})
hc : Heat capacitance
nf : Nanofluid
hnf : Hybrid nanofluid
bf : Base fluid
TC : Thermal conductivity
HT : Heat transfer
HTR : Heat transfer rate
BLF : Boundary layer flow
EG : Entropy generation
PDE : Partial differential equation
NLTR : Nonlinear thermal radiation
VBLT : Velocity boundary layer thickness
TBLT : Thermal boundary layer thickness
AF : Assisting flow
OF : Opposing flow
ρ_{hnf}, ρ_{nf}, ρ_f, ρ_{n_1}, ρ_{n_2} : Effective density of the hnf, nf, bf, Al_2O_3, Cu ($kg\ m^{-3}$)
$(\rho C_p)_{hnf}$, $(\rho C_p)_{nf}$, $(\rho C_p)_f$, $(\rho C_p)_{n_1}$, $(\rho C_p)_{n_2}$: HC of the hnf, nf, bf, Al_2O_3, Cu ($J\ kg^2\ m^3\ K^{-1}$)
μ_{hnf}, μ_{nf}, μ_f : Effective dynamic viscosity of the hnf, nf, bf ($kg\ m^{-1}\ s^{-1}$)
β_{hnf}, β_{nf}, β_f, β_{n_1}, β_{n_2} : Thermal expansion of hnf, nf, Al_2O_3, Cu (K^{-1})
k_{hnf}, k_{nf}, k_f, k_{n_1}, k_{n_2} : Tc of hnf, nf, Al_2O_3, Cu ($W\ m^{-1}\ K^{-1}$)
υ_{hnf}, υ_{nf}, υ_f : Kinematic viscosity of hnf, nf, bf (m^2s^{-1})
σ^* : Stefan-Boltzmann constant

*Corresponding author: Tel: +92-335-9761475
Fax: +92-335-9761475, e-mail: mikhan@math.qau.edu.pk

k^* : Mean absorption coefficient
K : Porous medium permeability
ϕ_1, ϕ_2 : Solid volume fraction for Al_2O_3, Cu
T : Fluid temperature in the boundary layer (K)
T_w : Temperature on the surface of cylinder (K)
T_∞ : Ambient fluid temperature (K)

$\lambda = \frac{g\beta T_\infty(\theta_r - 1)x}{U_0^2}$: Mixed convection parameter

$\mathrm{Re} = \frac{U_0 x}{\upsilon_f}$: Reynolds number

$\beta = \frac{\upsilon_f l}{KU_0}$: Porosity parameter

U_0 : Constant velocity

$\mathrm{Pr} = \frac{\upsilon_f}{\alpha_f}$: Prandtl number

$\Omega = \sqrt{\frac{l\upsilon_f}{U_0 a^2}}$: Curvature parameter

l : Length

$N_R = \frac{k^* k_f}{4\sigma^* T_\infty^3}$: Radiation parameter

$E_c = \frac{U_0^2}{T_\infty(\theta_r - 1)(c_p)_f}$: Eckert number

$\Lambda = \frac{x}{l}$: Dimensionless length ratio parameter

$Br = \mathrm{Pr}.Ec = Br$

$= \frac{\mu_f U_0^2}{k_f T_\infty(\theta_r - 1)}$: Brinkman number

$\theta_r = \frac{T_w}{T_\infty}$: Temperature ratio parameter

$S_0''' = \frac{k_f(\theta_r - 1)^2}{l^2}$: Non-dimensional characteristic EG rate

Suffixes

hnf : Hybrid nanofluid
nf : Nanofluid
f : Base fluid
n_1 : Nanoparticle Al_2O_3
n_2 : Nanoparticle Cu

1. Introduction

Thermal distribution has important notable uses in the industrial and engineering industries. In many engineering products such as electrical equipment, nuclear cooling systems, heat exchangers and mechanical applications we use traditional liquids as a heat carrier. Due to its low capacity of thermal distribution, addition of nanosized particles with base liquid leads to new type of liquid called nanofluids. A new kind of fluid show high thermal distribution rate when compared to base fluids. Choi and Eastman [1] proposed the notion of nanofluids and established that they improve heat conductivity more than basic liquids. Some of the noteworthy recent works on nanofluids are [2-5]. In addition, with the base fluid, two different kinds of mixtures are combined, and the thermal performance has increased considerably compared to nano- and base fluids. Many researchers did a lot of work on hybrid nanofluids. Recently, Chu *et al.* [6] examined the photocatalytic treatment of lignin in the presence of hybrid nanoparticles for the production of methane in lab scale continuous reactors. Madhukesh *et al.* [7] investigated the Aluminium water-based hybrid nanofluid flow in curved stretching sheet. Farooq *et al.* [8] studied the peristaltic activity of hybrid type nanoparticles viscous fluid in the presence of non linear radiation and slip effects. Gowda *et al.* [9] analysed the hybrid carbon nanotube flow over upward-downward moving rotating disk. Ramesh *et al.* [10] explored the Bodewadt flow and thermal analysis in the presence of hybrid nanofluid flow.

The fluid rheology, which explains the fluid's nature and shear stress, aids in the classification of liquids. Fluids are divided into non-Newtonian and Newtonian fluid models based on their rheology. Newtonian fluids follow Newton's law, while non-Newtonian fluids have many rheological characteristics that cannot be represented in a single productive equation. We acquire many rheological models of non-Newtonian fluid provided by many investigators in order to express the non-Newtonian fluid. The Casson fluid model is one of the most widely researched fluid models. Recently, Ahmad and Nadeem [11] investigated the CCHF of single and multiwall carbon nanotubes in the presence of Casson hybrid nanofluids over a lubricated surface. Jyothi *et al.* [12] examined the time dependent flow of Casson hybrid nanofluid flow with thermophoretic particle deposition over a parallel plate. Alghamdi *et al.* [13] have explored the Casson hybrid nanofluid boundary layer stagnation point flow on unstable stretched sheets. Madhukesh *et al.* [14] considered the thermal and mass transfer aspects of Casson hybrid nanofluid flow over a Riga plate. The suction effects of instable Casson hybrid nano liquid were examined by Kamis *et al.* [15] across a stretching surface.

One of the key features of many industrial sectors is a research on thin needles. Many scholars investigate exten-

sively the topic of heat distribution and flow under various circumstances. Major applications include thermocouple hot wire anemometer for wind speed measurement, microscale heat extraction cooling systems, electronic microstructure equipping that leads to very precise and efficient measurement, etc. Recently, Salleh *et al.* [16] studied the Buoyancy force on thermal distribution around a thin needle in the presence of hybrid nanofluid flow. Kumar *et al.* [17] examined the thermophoretic particle deposition and thermal distribution considering Casson fluid. Waini *et al.* [18] determined the moment of hybrid nano liquid low over a permeable moving thin needle. Tili *et al.* [19] elaborated the effect of resistive heating over a poignant thin needle in a MHD Sakiadis hybrid nanofluid flow. The flow and thermal study of moving nanofluid near the constantly moving needle was examined by Hashim *et al.* [20].

The fluid flow across a permeable area is estimated by Henry Darcy [21], based on the results of water flow studies over sand and sand pits and hydrogeology. In 1856 he established his notion of a spongy medium fluid flow. Philipp's Forchheimer's [22] modification of the momentum equation by speed square v^2 in Darcian speed was due to its restrictions on small speed with lower permeability. As a result, this term is known as Forchheimer term. Khan *et al.* [23] determined the Marangoni convective flow of hybrid nanofluid in the presence of Darcy Forchheimer medium. Xiong *et al.* [24] examined the multiple solutions of Darcy Forchheimer saturated flow over a cross nanofluid in vertical thin needle. Ramesh *et al.* [25] investigated the thermal distribution of hybrid liquid in thin needle in the presence of Darcy Forchheimer medium.

Buongiorno [26] suggested a model in 2006 to strengthen the homogeneous single phase and thermal dispersion models. Buongiorno investigated the impact of seven slip processes include inertia, thermophoresis, Brownian diffusion, magnus effect, diffusiophoresis, gravity and fluid drainage. Among these he concluded thermophoresis and Brownian diffusion are important slip mechanism found in nanofluids. Recently, Rana *et al.* [27] considered the three-dimensional flow and thermal distribution of nanofluid with radiative heat flux and convective thermal conditions by using modified Buongiorno model. Ijaz *et al.* [28] analysed the entropy generation of nonlinearly convective flow of Sisko fluid in the presence of joule heating and activation energy using Buongiorno model. Turkyilmazoglu [29] studied the transparent effects of Buongiorno model of nanofluid on heat and mass transfer.

Thermal radiation is one of the significant applications in context with the flow process. The thermal radiation effect is crucial in the design of trustworthy equipment, nuclear power stations, jet engines, and other propulsion mechanisms for spacecrafts, weapons, and satellites, heat controlling in polymer industries, as well as many complex convection systems. In view of these applications, many researchers have conducted studies on thermal radiation. Recently, Aziz *et al.* [30] considered the thermal distribution and entropy analysis of Maxwell hybrid nanofluid flow including thermal radiation and joule heating. Wahid *et al.* [31] examined the MHD Darcy slip flow of Viscoelastic fluid over a slippery surface in the presence of thermal radiation and viscous dissipation. Sreedevi *et al.* [32] investigated the unsteady hybrid nanofluid flow over a stretching surface by considering thermal radiation. Madhukesh *et al.* [33] studied the Bio Marangoni convective flow of Casson nanofluid flow in a porous medium in the presence of activation energy. Refs. [34-40] examines the impact of fluid flow with nano and without nanofluids.

Based on the above affordable literature survey, no study has been conducted on Casson hybrid nanofluid flow over a thin needle to analyse the entropy generation and Arrhenius pre-exponential factor law in the presence of Darcy Forchheimer medium. The present work examines Casson hybrid nanofluid flow over a thin needle for the entropy creation and the pre-exponential factor law in Darcy Forchheimer medium. The numerical results are obtained for different dimensionless constraints and discussed in detail with the help of plots.

2. Mathematical Description and Equations of the Physical Model

In the present problem we consider a steady, laminar boundary layer flow over a thin needle moving with a constant velocity U_w in a parallel free stream. A steady mixed convection flow of hybrid nanofluid comprising water as base fluid and copper and alumina as nanoparticles is considered. Darcy-Forchheimer flow model is implemented. It is essentially assumed that the thickness of the needle is comparable to or smaller than that of the momentum and thermal boundary layers over it. Pressure gradient along the needle is neglected and $r = R(x)$ is the radius of the needle, where r and x represent the radial and axial coordinates. A schematic diagram imparting physical description of the problem is shown in Fig. 1.

Under the above assumptions, the resulting equations of non-Newtonian nanofluids flow over thin needle are

$$\frac{\partial}{\partial x}(ru) + \frac{\partial}{\partial r}(rv) = 0, \tag{1}$$

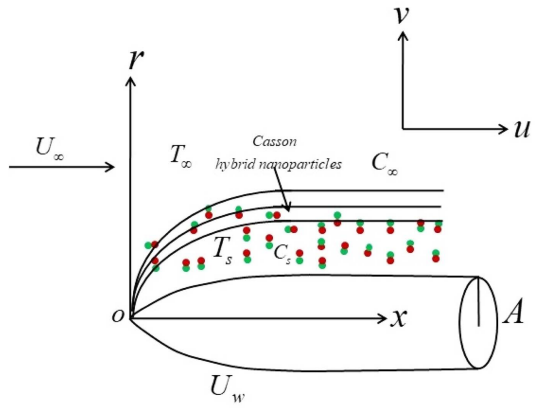

Fig. 1. (Color online) Schematic flow diagram.

$$u\frac{\partial u}{\partial x}+v\frac{\partial u}{\partial r}=\left(1+\frac{1}{\beta}\right)\frac{\mu_{hnf}}{\rho_{hnf}}\left(\frac{\partial^2 u}{\partial r^2}+\frac{1}{r}\frac{\partial u}{\partial r}\right)+g\frac{(\rho\beta)_{hnf}}{\rho_{hnf}}(T-T_\infty)-\left(1+\frac{1}{\beta}\right)\frac{\mu_{hnf}u}{\rho_{hnf}K}-Fu^2 \tag{2}$$

$$u\frac{\partial T}{\partial x}+v\frac{\partial T}{\partial r}+\delta_E\left(\begin{array}{l}u^2\frac{\partial^2 T}{\partial x^2}+v^2\frac{\partial^2 T}{\partial r^2}+2uv\frac{\partial^2 T}{\partial r\partial x}+u\frac{\partial u}{\partial x}\frac{\partial T}{\partial x}\\+u\frac{\partial v}{\partial x}\frac{\partial T}{\partial r}+v\frac{\partial u}{\partial r}\frac{\partial T}{\partial x}+v\frac{\partial v}{\partial r}\frac{\partial T}{\partial r}\end{array}\right)$$
$$=\alpha_{hnf}\frac{1}{r}\frac{\partial}{\partial r}\left(r\frac{\partial T}{\partial r}\right)+\frac{(\rho c_p)_p}{(\rho c_p)_{hnf}}\left[D_B\frac{\partial T}{\partial r}\frac{\partial C}{\partial r}+\frac{D_T}{T_\infty}\left(\frac{\partial T}{\partial r}\right)^2\right]$$
$$+\frac{16\sigma^* T_\infty^3}{3k^*(\rho c_p)_{hnf}}\frac{\partial^2 T}{\partial r^2}+\left(1+\frac{1}{\beta}\right)\frac{\mu_{hnf}}{(\rho c_p)_{hnf}}\left(\frac{\partial u}{\partial r}\right)^2$$
$$+\left(1+\frac{1}{\beta}\right)\frac{\mu_{hnf}}{(\rho c_p)_{hnf}}\frac{u^2}{K}+\frac{\rho_{hnf}F}{(\rho c_p)_{hnf}}u^3 \tag{3}$$

$$u\frac{\partial C}{\partial x}+v\frac{\partial C}{\partial r}+\delta_C\left(\begin{array}{l}u^2\frac{\partial^2 C}{\partial x^2}+v^2\frac{\partial^2 C}{\partial r^2}+2uv\frac{\partial^2 C}{\partial r\partial x}+u\frac{\partial u}{\partial x}\frac{\partial C}{\partial x}\\+u\frac{\partial v}{\partial x}\frac{\partial C}{\partial r}+v\frac{\partial u}{\partial r}\frac{\partial C}{\partial x}+v\frac{\partial v}{\partial r}\frac{\partial C}{\partial r}\end{array}\right)$$
$$=\frac{D_B}{r}\frac{\partial}{\partial r}\left(r\frac{\partial C}{\partial r}\right)+\frac{D_T}{T_\infty}\frac{1}{r}\frac{\partial}{\partial r}\left(r\frac{\partial T}{\partial r}\right)$$
$$\underbrace{-k_r^2\left(\frac{T}{T_\infty}\right)^m\exp\left(-\frac{E_a}{k_B T}\right)(C-C_\infty)}_{Arrhenius\ pre\text{–}exponential\ factor\ law} \tag{4}$$

Boundary conditions:

$$\left.\begin{array}{c}u\big|_{r=R}=u_w, v\big|_{r=R}=0,\\-k\frac{\partial T}{\partial r}=h_T(T_s-T)\big|_{r=R}, -k\frac{\partial C}{\partial r}=h_C(C_s-C)\big|_{r=R}\\u\big|_{r\to\infty}=u_\infty,\ T\big|_{r\to\infty}\to T_\infty=dx+T_0,\ C\big|_{r\to\infty}\to C_\infty=ex+C_0,\end{array}\right\} \tag{5}$$

here h_1 and h_2 stand for heat and mass transfer coefficients, $T_s=ax+T_0, C_s=bx+C_0$ for surface temperature-concentration and $T_\infty=dx+T_0, C_\infty=ex+C_0$ for ambient temperature-concentration respectively.

The suitable transformations are

$$\left.\begin{array}{l}u=2Uf'(\eta),\ v=-\frac{\upsilon_f}{r}f+\eta\frac{\upsilon_f}{r}f'(\eta),\\\theta(\eta)=\frac{T-T_\infty}{T_s-T_0}, \phi(\eta)=\frac{C-C_\infty}{C_s-C_0},\ \eta=\frac{Ur^2}{\upsilon_f x}\end{array}\right\} \tag{6}$$

where velocities u and v satisfy Eq. (1) identically. By letting $\eta=A$ in the Eq. (6), we have $R(x)=\left(\frac{Avx}{U}\right)^{1/2}$ is the surface shape of axisymmetric body.

The physical properties of the hybrid nanofluid and the applied models are defined as

Density $$\rho_{hnf}=(1-\phi)\rho_{bf}+\phi_{Cu}\rho_{Cu}+\phi_{Al_2O_3}\rho_{Al_2O_3} \tag{7}$$

Heat capacitance
$$(\rho C_p)_{hnf}=(1-\phi)(\rho C_p)_{bf}+\phi_{Cu}(\rho C_p)_{Cu}+\phi_{Al_2O_3}(\rho C_p)_{Al_2O_3} \tag{8}$$

Thermal expansion coefficient
$$(\rho\beta)_{hnf}=(1-\phi)(\rho\beta)_{bf}+\phi_{Cu}(\rho\beta)_{Cu}+\phi_{Al_2O_3}(\rho\beta)_{Al_2O_3} \tag{9}$$

Thermal diffusivity $$\alpha_{hnf}=\frac{k_{hnf}}{(\rho C_p)_{hnf}} \tag{10}$$

Dynamic viscosity $$\frac{\mu_{hnf}}{\mu_{bf}}=\frac{1}{\left(1-(\phi_{cu}+\phi_{Al_2}O_3)\right)^{2.5}} \tag{11}$$

And the thermal conductivity of hybrid nanofluid is defined by

$$\frac{k_{hnf}}{k_f}=\frac{\left(\frac{\phi_{Al_2O_3}k_{Al_2O_3}+\phi_{Cu}k_{Cu}}{\phi}\right)+2k_{bf}+2(\phi_{Al_2O_3}k_{Al_2O_3}+\phi_{Cu}k_{Cu})-2\phi k_{bf}}{\left(\frac{\phi_{Al_2O_3}k_{Al_2O_3}+\phi_{Cu}k_{Cu}}{\phi}\right)+2k_{bf}-(\phi_{Al_2O_3}k_{Al_2O_3}+\phi_{Cu}k_{Cu})+\phi k_{bf}} \tag{12}$$

Using Eqs. (6-12) in Eqs. (2)-(5), we get

$$8\delta_1\left(1+\frac{1}{\beta}\right)(f''+\eta f''')+4ff''+\delta_2\lambda\theta$$
$$-2\delta_1\left(1+\frac{1}{\beta}\right)\Omega f'-4F_r(f')^2=0 \tag{13}$$

$$\frac{k_{hnf}}{k_{bf}}\delta_3(2\theta'+2\eta\theta'')+\Pr f\theta'$$
$$-\Pr\omega_E\left\{\begin{array}{l}4\eta^2(f')^2\theta''+4\eta(f')^2\theta''-4\eta f f'\theta''\\+2\eta\lambda f f'\theta''-3\eta f^2\theta'+\frac{2}{\eta}f^2\theta'\end{array}\right\}$$

$$+\frac{8}{3Nr}\delta_3\eta\theta''+2\Pr\delta_3 Nb\eta\theta'\phi'+2\Pr\delta_3 Nt\eta(\theta')^2$$
$$+8\left(1+\frac{1}{\beta}\right)\eta Br\delta_4(f'')^2+2\left(1+\frac{1}{\beta}\right)\delta_4 Br\Omega(f')^2 \quad (14)$$
$$-4\delta_5 BrF_r(f')^3=0$$

$$2\phi'+2\eta\phi''+Sc\,f\phi'-Sc\,\omega_C\left\{\begin{matrix}4\eta^2(f')^2\phi''+4\eta(f')^2\phi''-4\eta f\,f'\phi''\\+2\eta\lambda f\,f'\phi''-3\eta f^2\phi'+\frac{2}{\eta}f^2\phi'\end{matrix}\right\} \quad (15)$$

with $+2\left(\frac{Nt}{Nb}\right)(\theta'+\eta\theta'')-\frac{1}{2}\Lambda Sc(1+\delta\theta)^m\exp\left[-\frac{E}{(1+\delta\theta)}\right]\phi=0$

$$\left.\begin{aligned}&f'(A)=\frac{\varepsilon}{2},f(A)=0,\\&\theta'(A)=-\frac{1}{2}\beta_T\left[1-S_T-\theta(A)\right],\phi'(A)=-\frac{1}{2}\beta_C\left[1-S_C-\phi(A)\right],\\&f'(\infty)=\frac{1}{2}(1-\varepsilon),g'(\infty)=0,\ \theta(\infty)\to 0,\ \phi(\infty)\to 0\end{aligned}\right\} \quad (16)$$

In the above expressions, the involved interesting parameters are defined by

$$\left.\begin{aligned}&\mathrm{Re}_x=\frac{Ux}{\upsilon_{bf}},\lambda=\frac{g\beta_{bf}(T_s-T_0)x}{U_0^2},Sc=\frac{\upsilon_f}{D_B},F_r=Fx,\Omega=\frac{\upsilon_{bf}x}{KU_0},\\&Nr=\frac{k^*k_{bf}^*}{4\sigma^*T_\infty^3},\delta=\frac{T_s-T_0}{T_\infty},\omega_E=\frac{\delta_E U}{x},\omega_C=\frac{\delta_C U}{x},\Pr=\frac{\upsilon_{bf}}{\alpha_{bf}},\lambda=\frac{r}{x},\\&Nt=\frac{\tau D_T(T_s-T_0)}{\upsilon_{bf}T_\infty},Nb=\frac{\tau D_B(C_s-C_0)}{\upsilon_{bf}},E_c=\frac{U^2}{(c_p)_f(T_s-T_0)},Br=\Pr Ec,\\&E=\frac{E_a}{k_BT_\infty},\Lambda=\frac{xk_r^2}{U},\varepsilon=\frac{u_w}{U},S_T=\frac{d}{a},S_C=\frac{b}{e},\beta_T=\frac{h_T}{k\left(\frac{Ur}{\upsilon x}\right)},\beta_C=\frac{h_C}{k\left(\frac{Ur}{\upsilon x}\right)}.\end{aligned}\right\} \quad (17)$$

With $\delta_1=\dfrac{1}{(1-\phi_{Al_2O_3}-\phi_{Cu})^{2.5}\left[(1-\phi)+\phi_{Cu}\left(\frac{\rho_{Cu}}{\rho_{bf}}\right)+\phi_{Al_2O_3}\left(\frac{\rho_{Al_2O_3}}{\rho_{bf}}\right)\right]}$,

$$\delta_2=\frac{(1-\phi)+\phi_{Cu}\left(\frac{(\rho\beta)_{Cu}}{(\rho\beta)_{bf}}\right)+\phi_{Al_2O_3}\left(\frac{(\rho\beta)_{Al_2O_3}}{(\rho\beta)_{bf}}\right)}{\left[(1-\phi)+\phi_{Cu}\left(\frac{\rho_{Cu}}{\rho_{bf}}\right)+\phi_{Al_2O_3}\left(\frac{\rho_{Al_2O_3}}{\rho_{bf}}\right)\right]},$$

$$\delta_3=\frac{1}{(1-\phi)+\phi_{Cu}\left(\frac{(\rho C_p)_{Cu}}{(\rho C_p)_{bf}}\right)+\phi_{Al_2O_3}\left(\frac{(\rho C_p)_{Al_2O_3}}{(\rho C_p)_{bf}}\right)},$$

$$\delta_4=\frac{1}{(1-\phi_{Al_2O_3}-\phi_{Cu})^{2.5}\left[(1-\phi)+\phi_{Cu}\left(\frac{(\rho C_p)_{Cu}}{(\rho C_p)_{bf}}\right)+\phi_{Al_2O_3}\left(\frac{(\rho C_p)_{Al_2O_3}}{(\rho C_p)_{bf}}\right)\right]},$$

$$\delta_5=\frac{(1-\phi)+\phi_{Cu}\left(\frac{\rho_{Cu}}{\rho_{bf}}\right)+\phi_{Al_2O_3}\left(\frac{\rho_{Al_2O_3}}{\rho_{bf}}\right)}{\left[(1-\phi)+\phi_{Cu}\left(\frac{(\rho C_p)_{Cu}}{(\rho C_p)_{bf}}\right)+\phi_{Al_2O_3}\left(\frac{(\rho C_p)_{Al_2O_3}}{(\rho C_p)_{bf}}\right)\right]}$$

The dimensionless local skin friction is defined by

$$\mathrm{Re}_x^{\frac{1}{2}}C_{fx}=4\left(1+\frac{1}{\beta}\right)\frac{f''(A)}{(1-\phi_{Al_2O_3}-\phi_{Cu})^{2.5}}A^{\frac{1}{2}} \quad (18)$$

in which the local Reynolds number is defined by $\mathrm{Re}_x=\dfrac{Ux}{\upsilon}$.

3. Entropy Production Analysis

3.1. The local entropy generations (EG)

$$\dot{S}_{gen}'''=\underbrace{\frac{k_{bf}}{T^2}\left[\frac{k_{hnf}}{k_{bf}}+\frac{16\sigma^*T_\infty^3}{3k^*k_{bf}}\right]\left(\frac{\partial T}{\partial r}\right)^2}_{\text{Thermal conduction irreversibility}}+\underbrace{\frac{\mu_{hnf}}{T}\left(\frac{\partial u}{\partial r}\right)^2}_{\text{Viscous dissipation irreversibility}}$$
$$+\underbrace{\frac{\mu_{hnf}u^2}{TK}+\frac{\rho_{hnf}F}{T}u^3}_{\text{Porous medium Irrriversibility}}+\underbrace{\frac{RD_B}{T}\left(\frac{\partial C}{\partial r}\frac{\partial T}{\partial r}\right)+\frac{RD_B}{C}\left(\frac{\partial C}{\partial r}\right)^2}_{\text{Mass transfer irreversibility}} \quad (19)$$

Here, R is the molar gas constant, F is the inertia coefficient in the porous medium, D_B is the molecular diffusion coefficient and K is the porous medium permeability.

The dimensionless EG rate N_G becomes:

$$N_G=\frac{S_{gen}'''}{S_0'''}$$
$$=4\left(\frac{k_{hnf}}{k_{bf}}+\frac{4}{3Nr}\right)\frac{\mathrm{Re}^2}{(1+\delta)^2}(\theta')^2+\frac{16}{(1-\phi_{Cu}-\phi_{Al_2O_3})^{2.5}}\frac{Br\,\mathrm{Re}^2}{\delta(1+\delta)}(f'')^2$$
$$+\frac{4}{(1-\phi_{Cu}-\phi_{Al_2O_3})^{2.5}}\frac{Br}{\delta(1+\delta)}(f')^2+4\frac{\Gamma\mathrm{Re}^2}{\delta(1+\delta)}\theta'\phi'+4\frac{\Gamma\delta^*\mathrm{Re}^2}{\delta^2(1+\delta^*)}(\phi')^2$$
$$+8\left[(1-\phi)+\phi_{Cu}\left(\frac{\rho_{Cu}}{\rho_{bf}}\right)+\phi_{Al_2O_3}\left(\frac{\rho_{Al_2O_3}}{\rho_{bf}}\right)\right]\frac{F_r Br\,\mathrm{Re}}{\delta(1+\delta)}(f')^3 \quad (20)$$

3.2. The Bejan number

$$Be=\frac{\left(\frac{k_{hnf}}{k_{bf}}+\frac{4}{3Nr}\right)\frac{\mathrm{Re}^2}{(1+\delta)^2}(\theta')^2+\frac{\Gamma\mathrm{Re}^2}{\delta(1+\delta)}\theta'\phi'+\frac{\Gamma\delta^*\mathrm{Re}^2}{\delta^2(1+\delta^*)}(\phi')^2}{\left(\frac{k_{hnf}}{k_{bf}}+\frac{4}{3Nr}\right)\frac{\mathrm{Re}^2}{(1+\delta)^2}(\theta')^2+\frac{4}{(1-\phi_{Cu}-\phi_{Al_2O_3})^{2.5}}\frac{Br\,\mathrm{Re}^2}{\delta(1+\delta)}(f'')^2}$$
$$+\frac{1}{(1-\phi_{Cu}-\phi_{Al_2O_3})^{2.5}}\frac{Br}{\delta(1+\delta)}(f')^2+\frac{\Gamma\mathrm{Re}^2}{\delta(1+\delta)}\theta'\phi'+\frac{\Gamma\delta^*\mathrm{Re}^2}{\delta^2(1+\delta^*)}(\phi')^2$$
$$+2\left[(1-\phi)+\phi_{Cu}\left(\frac{\rho_{Cu}}{\rho_{bf}}\right)+\phi_{Al_2O_3}\left(\frac{\rho_{Al_2O_3}}{\rho_{bf}}\right)\right]\frac{F_r Br\,\mathrm{Re}}{\delta(1+\delta)}(f')^3 \quad (21)$$

Table 1. Thermophysical properties of nanoparticles and water.

Properties	Al_2O_3	Cu	Water
ρ (kg/m^3)	3970	8933	997.1
c_p (J/kgK)	765	385	4179
k (W/mK)	40	401	0.613
$\beta\times 10^{-5}$ (K^{-1})	0.85	1.67	21
μ (kgm^{-1}s^{-1})	-	-	8.9×10^{-4}

4. Results and Discussion

This section explains the numerical and graphical outcomes of the various parameters on all of the gradients involved. The set of equations (13-15) with reduced boundary conditions (16) are numerically solved with the help of mathematical computational software with build in shooting technique and RKF45 method by utilizing thermophysical properties defined in (7-12) and material properties (Table 1) setting the error tolerance rate 10^{-6} and parameters ranges

$$\beta=10,\lambda=0.1,\omega=0.1,F_r=0.1,\mathrm{Pr}=10,\omega_E=0.1,$$
$$Nr=20,Nb=Nt=0.1,Br=1,Sc=2,\omega_C=0.1,$$
$$\Lambda=0.1,\delta=0.1,E=0.1,\epsilon=0.3,\beta_T=0.6,S_T=0.6,$$
$$S_C=0.6,\beta_C,\Gamma=0.1,\delta^*=0.1,Re=0.1,A=0.1,m=1.$$

The obtained results are well ordered with various dimensionless constraints with respective profiles.

4.1. Analysis of velocity profile for various constraints

Figures 2-5 depict the effect of several dimensionless variables on a velocity profile $f'(\eta)$, such as the porosity parameter (β), Darcy parameter (F_r), needle size (A), and velocity ratio parameter (ε). The variation of the porosity parameter over the velocity profile $f'(\eta)$ is depicted in Fig. 2. The fluid's velocity $f'(\eta)$ decreases as the porosity parameter increases. This is due to an increase in the porous medium size, which opposes the liquid's moment, lowering the fluid's velocity $f'(\eta)$. From the figure, the velocity of the hybrid nanofluid is greater than that of the nanofluid. Figure 3 is illustrated to draw the variation of axial velocity profile $f'(\eta)$ for different F_r. With increasing F_r values, the fluid's velocity drops. The inertial factor is very weak with upgradation of F_r values causes a decrease in fluid velocity. Velocity of the nanofluid is less than the velocity of the hybrid nanofluid. Figure 4 depicts the fluctuation of axial velocity $f'(\eta)$ with increasing values of thin needle size A. Up rise in the values of A will enhances the axial velocity $f'(\eta)$ profile. Physically, the lower size of the needle surface correlates to a weaker drag force that exists between the needle and

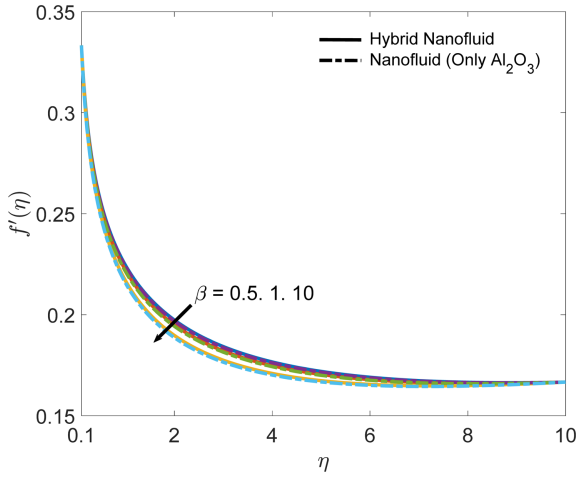

Fig. 2. (Color online) Axial velocity profile for different β with a comparison of hybrid nanofluid and nanofluid.

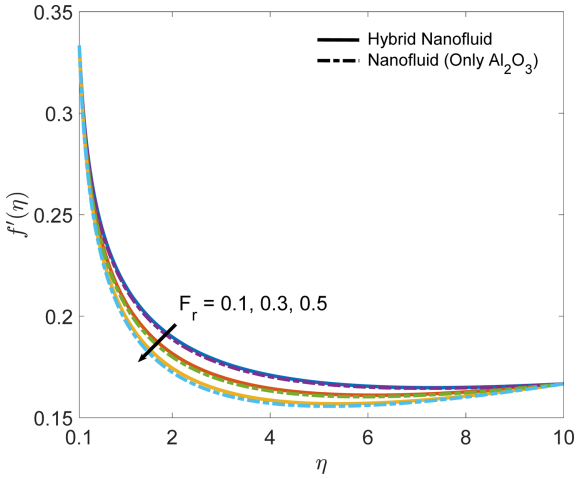

Fig. 3. (Color online) Axial velocity profile for different F_r with a comparison of hybrid nanofluid and nanofluid.

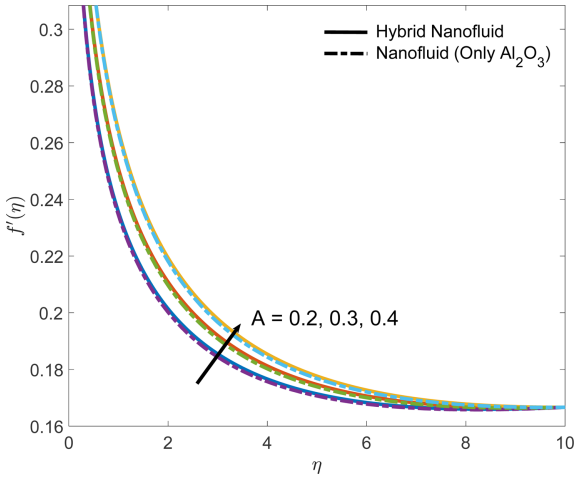

Fig. 4. (Color online) Axial velocity profile for different A with a comparison of hybrid nanofluid and nanofluid.

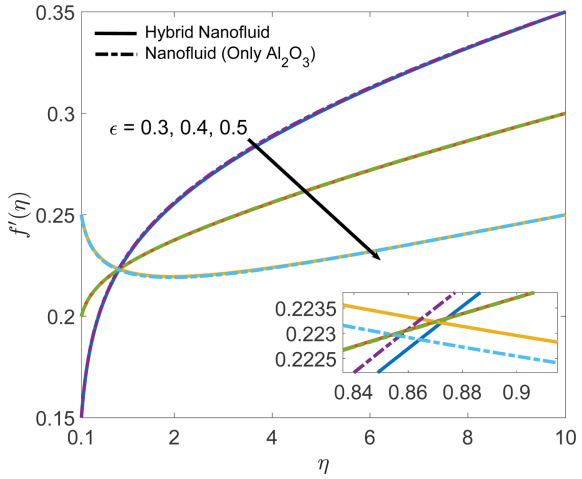

Fig. 5. (Color online) Axial velocity profile for different ε with a comparison of hybrid nanofluid and nanofluid.

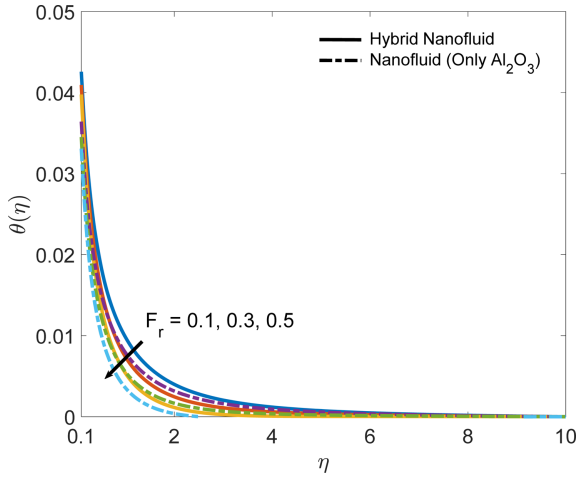

Fig. 7. (Color online) Temperature profile for different F_r with a comparison of hybrid nanofluid and nanofluid.

the fluid particles, resulting in an increase in fluid velocity. It is observed from the graph that velocity of the hybrid nanofluid is more than that of the nanofluid. Figure 5 outlines the impact of the velocity ratio parameter ε on the axial velocity profile $f'(\eta)$. The ratio of needle velocity and composite velocity is called velocity ratio parameter. The velocity profile decreases as the value of the velocity ratio parameter rises. When the needle in free stream, thickness of the boundary layer increases results in decrease in the axial velocity.

4.2. Analysis of temperature profile for various constraints

Figures 6-11 are illustrated to show the influence of porosity parameter (β), Darcy parameter (F_r), needle size (A), Prandtl number (Pr), ω_E, Brinkman number (B_r) on temperature profile $\theta(\eta)$. The influence of porosity parameter over is illustrated in the Fig. 6. The thermal distribution improves as the value of the porosity parameter rises. In physical terms, increasing the porous medium reduces the fluid's moment owing to drag force, resulting in improved heat distribution. Hybrid nanoliquid shows greater thermal performance than nanoliquid. Thermal distribution occurred due to influence of Darcy parameter is shown in the Fig. 7. Thermal distribution decreases with augmented values of (F_r). Temperature distribution is decreased against greater Forchheimer parameter values due to the decreasing inertia factor, which resists the fluid to flow. Nanoparticles have less thermal distribution than hybrid nanofluid. Figure 8 depicts the temperature profile fluctuation in the influence of needle size. As the size of the needle enhances thermal distribution significantly increases. Physically, the larger needle surface translates to a higher drag force between the needle and the fluid

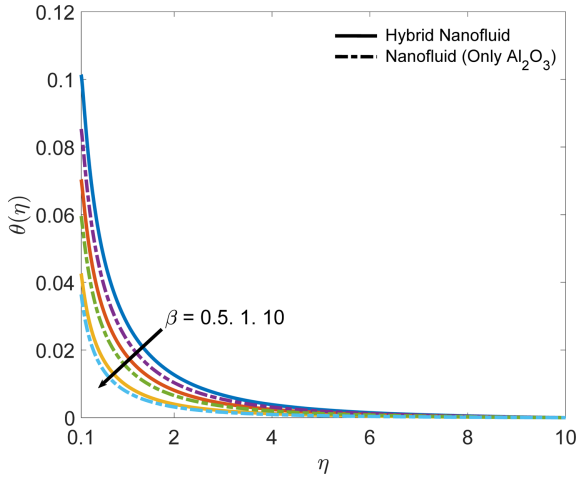

Fig. 6. (Color online) Temperature profile for different β with a comparison of hybrid nanofluid and nanofluid.

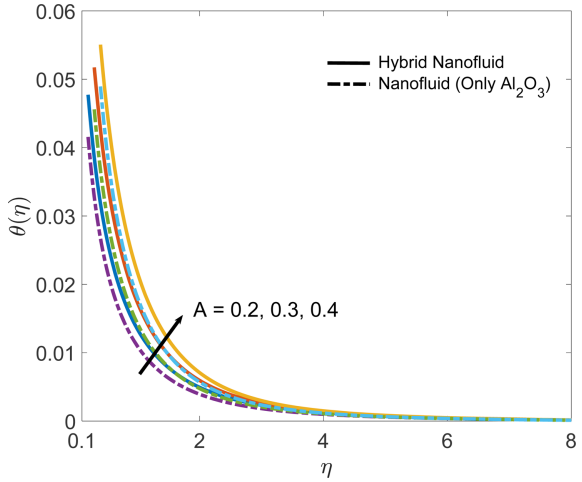

Fig. 8. (Color online) Temperature profile for different A with a comparison of hybrid nanofluid and nanofluid.

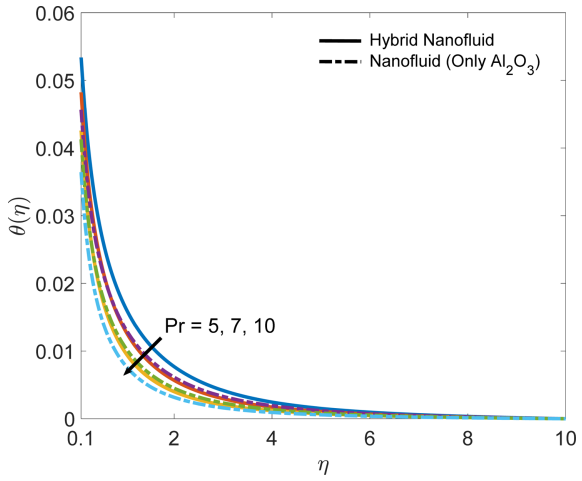

Fig. 9. (Color online) Temperature profile for different Pr with a comparison of hybrid nanofluid and nanofluid.

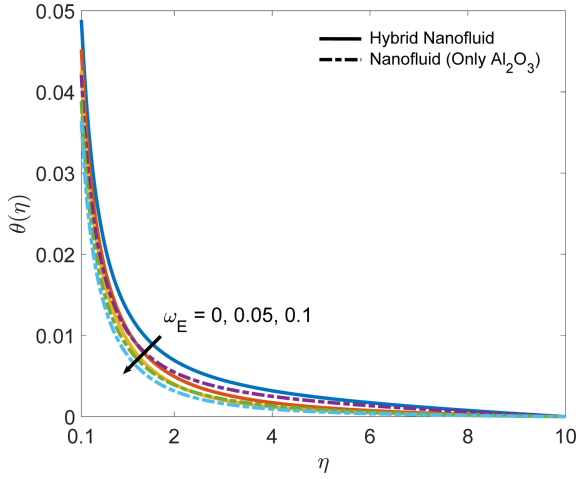

Fig. 10. (Color online) Temperature profile for different ω_E with a comparison of hybrid nanofluid and nanofluid.

particles, resulting in improved heat distribution. Furthermore, when the needle size grows larger, hybrid nanofluid outperforms nanofluid in terms of thermal performance. The variation of thermal profile for diverse values of Prandtl number is illustrated in the Fig. 9. As Prandtl number increases thermal performance declines. Thermal conductivity of the fluid declines as the Prandtl number increases which results in decrease in thermal curve. Thermal distribution is more in hybrid nanofluid case than nanofluid. Figure 10 is illustrated to draw the variation of thermal profile with respect to ω_E. Uplift in the values of ω_E will decrease the thermal profile. The presence of temperature difference factor gives time to exchange the thermal distribution between the molecules will reduces the thermal distribution.The discrepancy of thermal profile for various values of Brinkman number is shown in the Fig. 11. The Brinkman number is a dimensionless quantity that refers to heat transmission from a wall to a viscous fluid in motion. The heat dispersion rises as the Brinkman number scales up due to heat propagation between the surface and the fluid. In terms of thermal distribution, hybrid nanofluid has a bigger impact on Brinkman number than nanofluid, as seen in the Fig. 11.

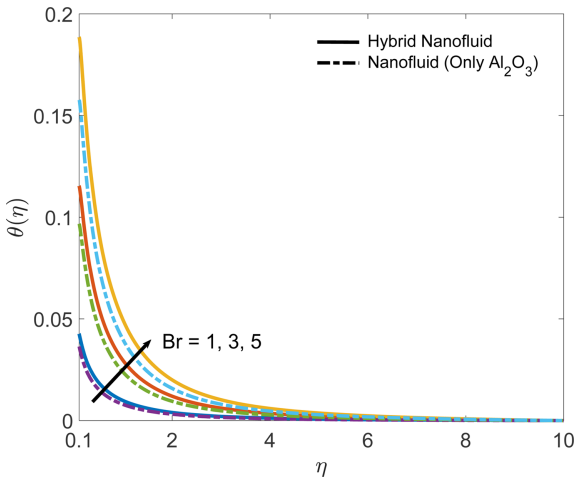

Fig. 11. (Color online) Temperature profile for different *Br* with a comparison of hybrid nanofluid and nanofluid.

4.3. Analysis of concentration profile for various constraints

The variation of concentration profiles for diverse parameters like porosity parameter (β), Darcy parameter (F_r), Brownian motion parameter (Nb), Thermophoresis parameter (Nt), Brinkman number (Br), Schmidt number (Sc), ω_c, dimensionless length ratio parameter (Λ), Activation energy parameter (E), The thermal expansion coefficient (β_T), S_T, S_C, The concentration expansion

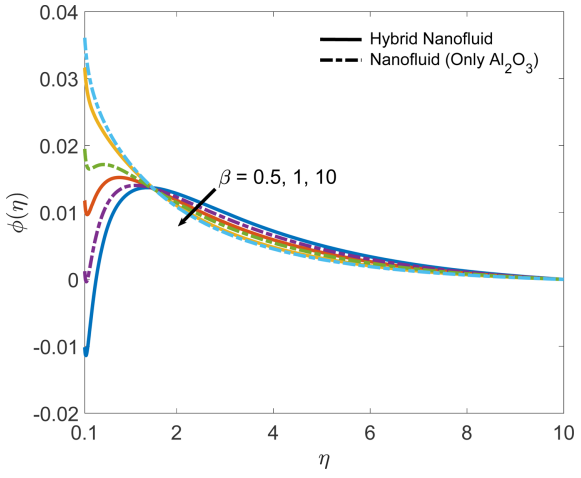

Fig. 12. (Color online) Concentration profile for different β with a comparison of hybrid nanofluid and nanofluid.

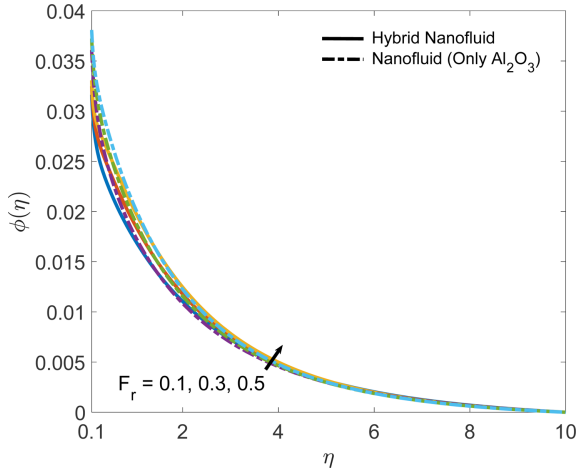

Fig. 13. (Color online) Concentration profile for different F_r with a comparison of hybrid nanofluid and nanofluid.

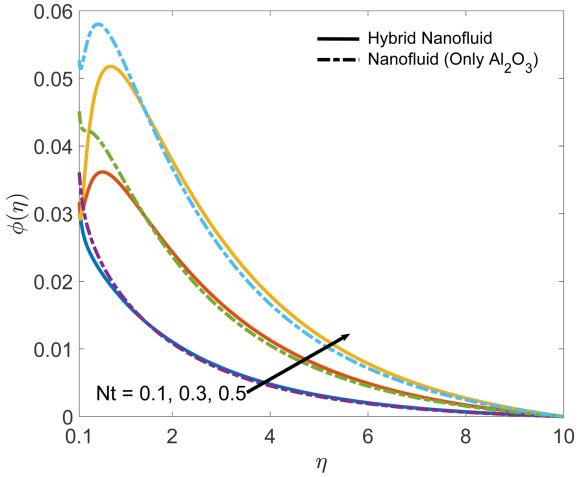

Fig. 15. (Color online) Concentration profile for different Nt with a comparison of hybrid nanofluid and nanofluid.

coefficient (β_C) are discussed via Figs. 12-24.

Figure 12 is illustrated to examine the variation of concentration profile over porosity parameter. Upsurge in the values of β increases the mass distribution at $0.1 < \eta < 2$. As $2 < \eta < 10$ the concentration of the fluid goes on decreases in the system. As physical point of view rise in the porosity parameter increases the thickness of the boundary layer and fluid moves far away from the needle reduces the mass distribution. Hybrid nanofluid shows more significant mass distribution than nanofluid. Figure 13 is drawn to show the variation of Darcy parameter over concentration profile. Concentration enhances with increase in the Darcy parameter. It is observed that nanofluid have a greater impact on mass distribution than hybrid nanofluid in the influence of Darcy parameter. The variation of concentration profile in the presence of Brownian motion parameter (Nb) and Thermophoresis parameter (Nt) is illustrated in the Figs. 14 and 15. Brownian motion is the random movement of nanofluid particles in an inconsistent manner. Brownian motion of nanofluids at the molecular scale has been proposed as a major mechanism governing nanofluid thermal conductivity. Increases in the Brownian parameter's values increase the nanoparticles' kinetic energy, resulting in a decrease in the concentration profile. Concentration of nanofluid is less than the hybrid nanofluid. Thermophoresis is a motion of nanoparticle brought by thermal gradients. escalating the values of thermophoresis parameter will enhance the concentration profile due to difference in the thermal gradients. Hybrid nanofluid concentration is more than nanofluid in the influence of thermophoresis parameter. Variation of concentration profile for diverse values of Brinkman number is illustrated in the Fig. 16. Brinkman number is a increasing function of concentration profile.

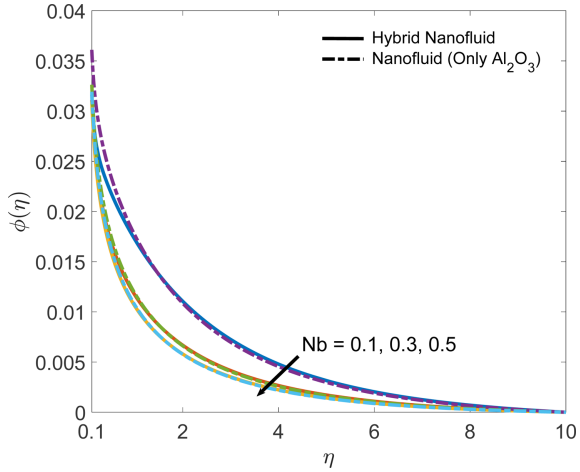

Fig. 14. (Color online) Concentration profile for different Nb with a comparison of hybrid nanofluid and nanofluid.

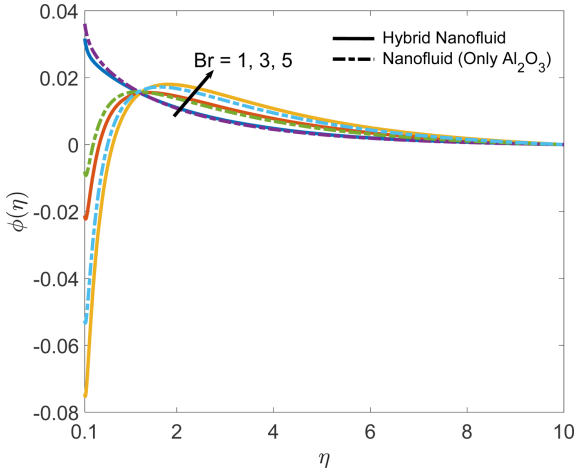

Fig. 16. (Color online) Concentration profile for different Br with a comparison of hybrid nanofluid and nanofluid.

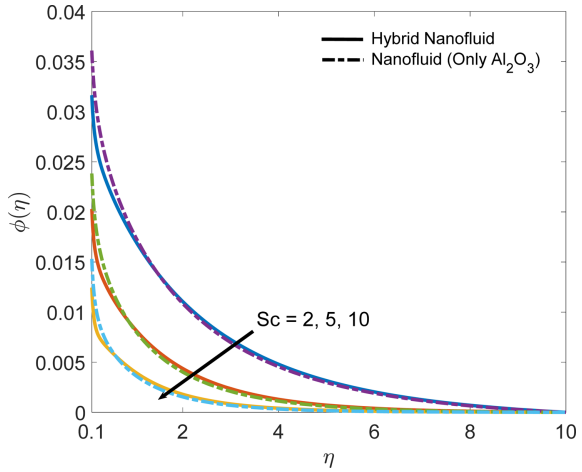

Fig. 17. (Color online) Concentration profile for different *Sc* with a comparison of hybrid nanofluid and nanofluid.

As the values of Brinkman number enhances the accumulation of particles to the surface increases which improves the concentration. Hybrid nanofluid shows greater impact in Brinkman number than nanofluid.

The influence of Schmidt number on concentration profile is shown in the Fig. 17. As Schmidt number improves concentration decreases. Hybrid nanofluid concentration is more than nanofluid in the influence of Schmidt number. In flows where both mass and momentum are diffused, the Schmidt number is a significant consideration. It physically connects the thickness of the hydrodynamic layer to the thickness of the mass transfer boundary layer. When the Schmidt number is increased in a fluid flow, the diffusion of momentum among particles in the fluid increases. This declines the concentration. Figure 18 illustrate the variation of ω_c over concentration profile. The rise in the values of ω_c will declines the

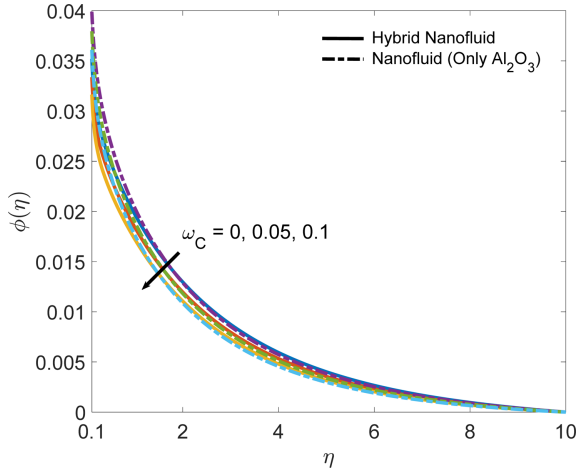

Fig. 18. (Color online) Concentration profile for different ω_C with a comparison of hybrid nanofluid and nanofluid.

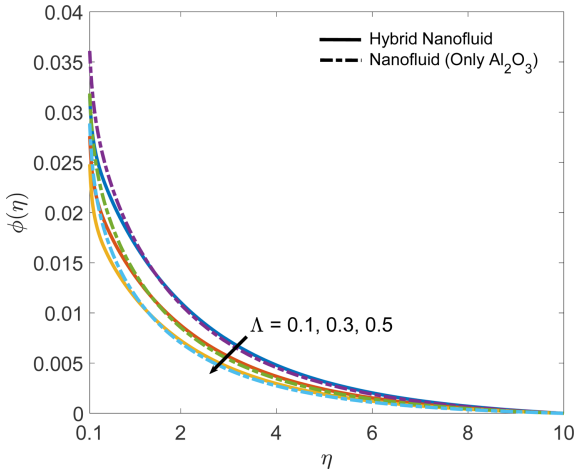

Fig. 19. (Color online) Concentration profile for different Λ with a comparison of hybrid nanofluid and nanofluid.

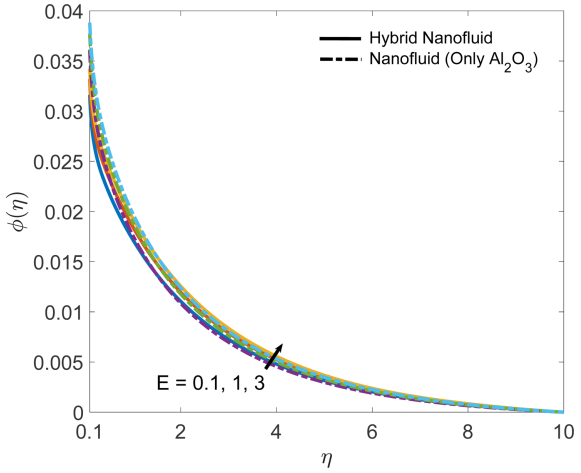

Fig. 20. (Color online) Concentration profile for different *E* with a comparison of hybrid nanofluid and nanofluid.

concentration. The impact of dimensionless length ratio parameter over concentration profile is drawn in the Fig. 19. The variation in Λ declines the concentration profile. As the values of Λ increases, more destructive chemical reactions occur, reducing the concentration of nanoparticles in the fluid flow. Hybrid nanofluid concentration is significantly high than nanofluid. Figure 20 illustrate the enhancement concentration profile for increasing values of activation energy parameter. Activation energy is the modified Arrhenius activation function. Rise in the values of *E* the function decays. As a result more amount of reaction takes place, concentration increases. The consequence of thermal expansion coefficient over concentration profile is drawn in the Fig. 21. Small rise in the values of β_T will enhance the concentration. Hybrid nanofluid exhibit higher concentration than nanofluid inn the variation of β_T. Figure 22 and 23 are drawn to show the influence of

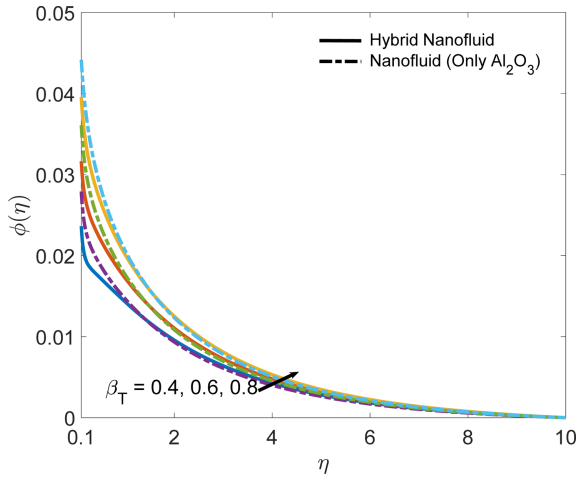

Fig. 21. (Color online) Concentration profile for different β_T with a comparison of hybrid nanofluid and nanofluid.

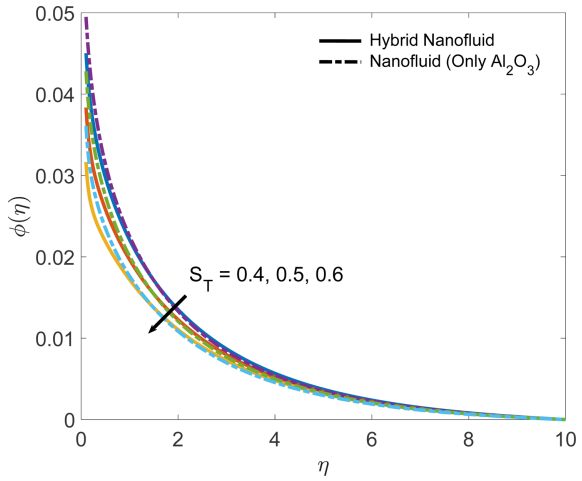

Fig. 22. (Color online) Concentration profile for different S_T with a comparison of hybrid nanofluid and nanofluid.

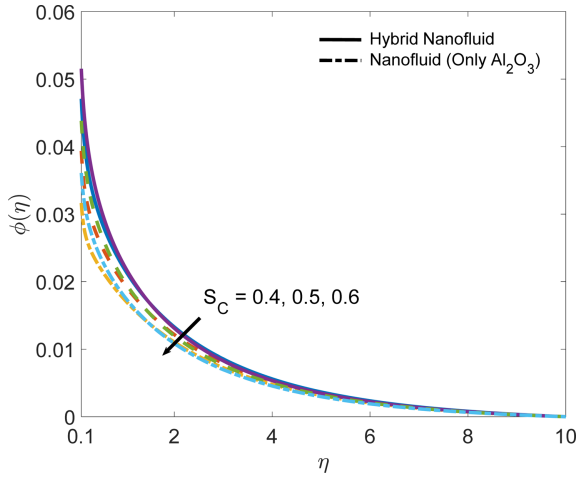

Fig. 23. (Color online) Concentration profile for different S_C with a comparison of hybrid nanofluid and nanofluid.

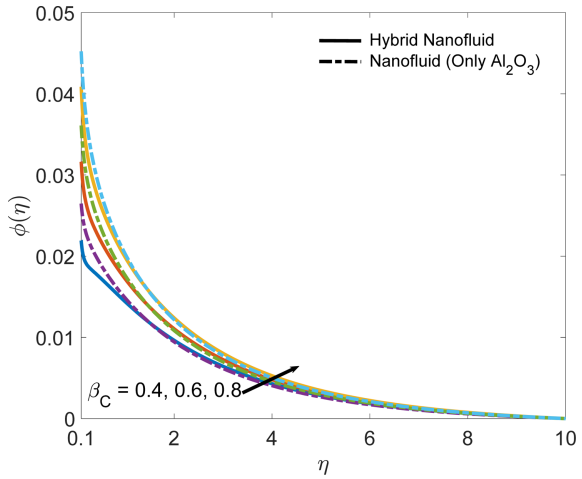

Fig. 24. (Color online) Concentration profile for different β_C with a comparison of hybrid nanofluid and nanofluid.

S_T and S_C parameters on concentration profiles. Heightening values of S_T and S_C parameters will declines the mass transfer profile. Figure 24 is portrayed to show the variation of concentration profile over various values of concentration expansion coefficient parameter β_C. Concentration profiles enriches with increase in the values of β_C.

4.4. Analysis of Skin Friction, Entropy Generation and Bejan number

Figure 25 represents the variation of surface drag force with size of the needle for diverse values of porous parameter. Rise in the values of porous parameter will enhances the surface drag force due to destruction caused by the porous medium for the flow. The reverse trend is seen in the case of Brinkman number and Darcy parameter (see Fig. 26). Surface drag force is more in case of

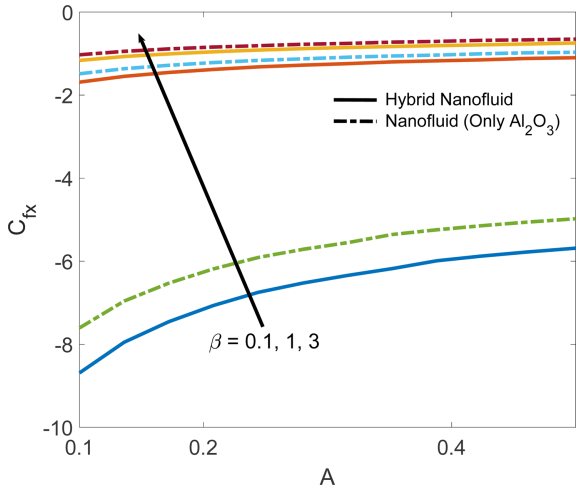

Fig. 25. (Color online) Skin friction vs. A for different β with a comparison of hybrid nanofluid and nanofluid.

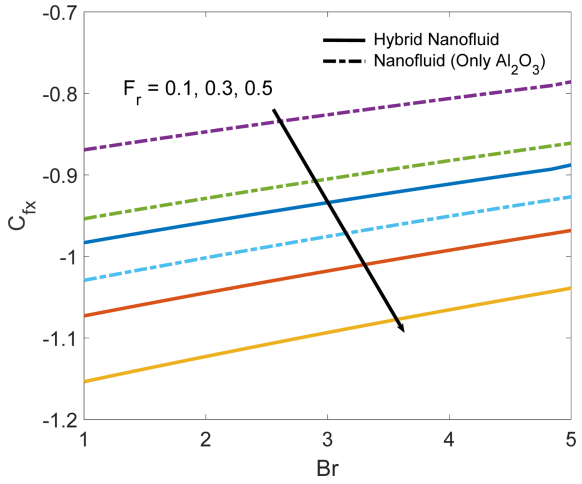

Fig. 26. (Color online) Skin friction vs. *Br* for different F_r with a comparison of hybrid nanofluid and nanofluid.

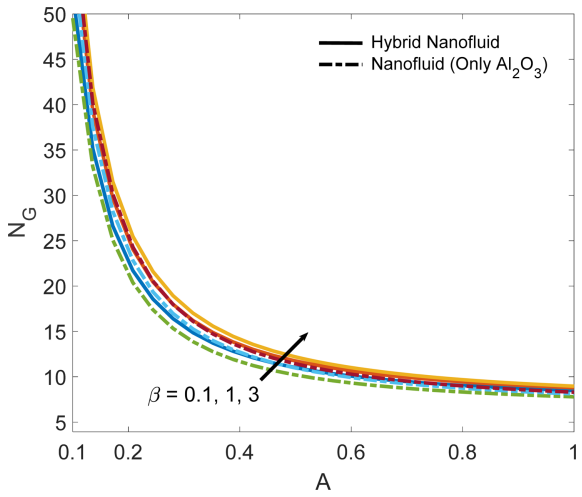

Fig. 27. (Color online) Entropy vs. *A* for different β with a comparison of hybrid nanofluid and nanofluid.

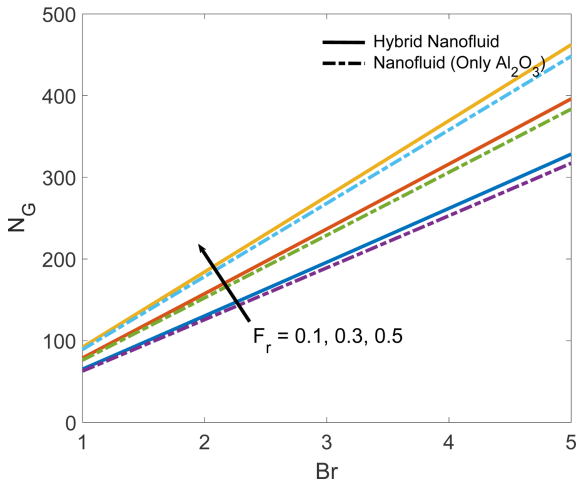

Fig. 28. (Color online) Entropy vs. *Br* for different F_r with a comparison of hybrid nanofluid and nanofluid.

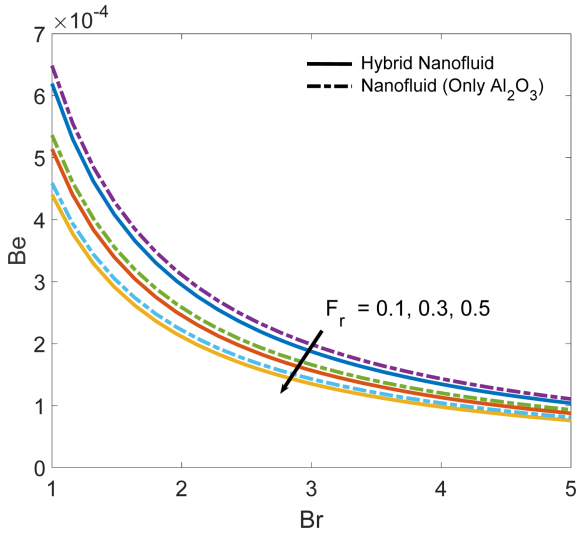

Fig. 29. (Color online) Bejan number vs. *Br* for different F_r with a comparison of hybrid nanofluid and nanofluid.

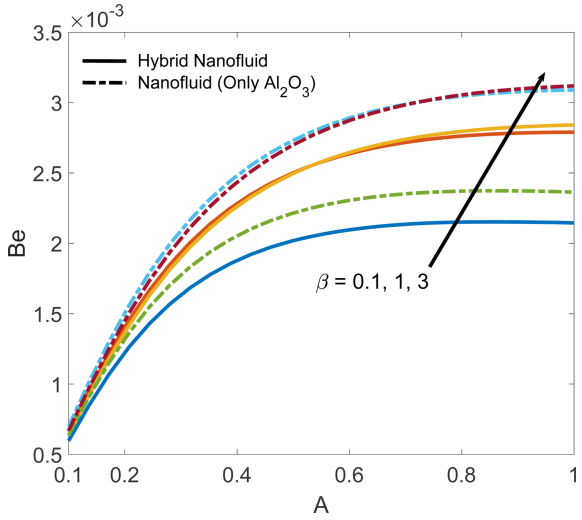

Fig. 30. (Color online) Bejan number vs. *A* for different β with a comparison of hybrid nanofluid and nanofluid.

nanofluid than hybrid one. Entropy generation N_G is discussed for various flow constraints A, β, Br and F_r is shown in the Figs. 27 and 28. Rise in the values of A and β will enhances the entropy generation in the system. Both parameters are important in the development of frictional forces, which result in irreversible fluid friction. Similar behaviour is observed in the case of Br and F_r parameters due to thermal transfer irreversibility (see Fig. 28). Entropy generation is high in hybrid nanofluid than nanofluid.

The variation of Bejan number for escalating values F_r of over Br is illustrated in the Fig. 29. Bejan number declines for increment in F_r as Darcy parameter will weakens the inertial factor. The influence of porosity

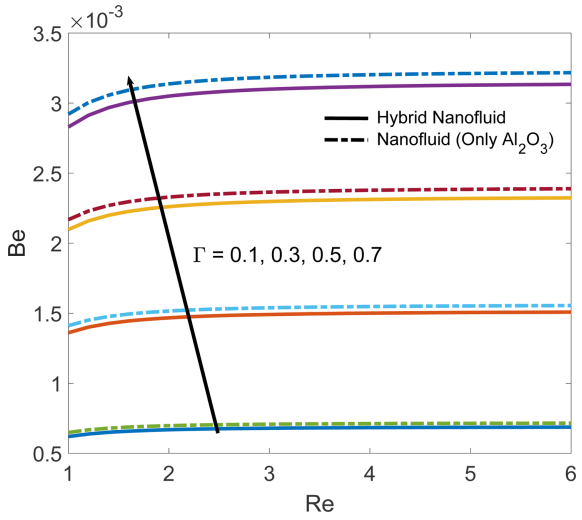

Fig. 31. (Color online) Bejan number vs. Re for different Γ with a comparison of hybrid nanofluid and nanofluid.

Table 2. Skin friction for different parameters. Values at the bracket represent the results with only Al_2O_3 nanoparticle.

β	λ	Ω	F_r	A	ε	$\sqrt{\mathrm{Re}_x}C_{fx}$
10	0.1	0.1	0.1	0.1	0.3	-0.98309548
						(-0.86918327)
0.1						-8.69015089
						(-7.60681849)
1						-1.68792733
						(-1.48602536)
	0.5					-0.98883202
						(-0.87533287)
	1					-0.99580848
						(-0.88281640)
		0.3				-1.27237513
						(-1.11985726)
		0.5				-1.50722891
						(-1.32397498)
			0.3			-1.07286340
						(-0.95371593)
			0.5			-1.15365282
						(-1.02927393)
				0.3		-0.75603719
						(-0.66965627)
				0.5		-0.68236205
						(-0.60478200)
					0.4	0.16483536
						(0.14344927)
					0.5	-0.26337230
						(-0.23410846)

parameter over Bejan number and needle size is dissipated in the Fig. 30. Enhancement in porosity will drags the fluid motion thickens the boundary layer as results Bejan number increases. Nanofluid shows greater impact on Bejan number than hybrid for escalation in porosity parameter. Further, the influence of Γ on Bejan number and Reynolds number is shown in the Fig. 31. From the Figs. 29-31 nanofluid performance is more than the hybrid one.

Table 2 is drawn to show the variation of Skin friction for various constraints for both nano and hybrid nanofluid. Table 3 shows the entropy generation and Bejan number for different parameters.

Table 3. Entropy generation and Bejan number for different parameters. Values at the bracket represent the results with only Al_2O_3 nanoparticle.

Nr	Re	δ	Γ	δ^*	Br	F_r	N_G	Be
20	1	0.1	0.1	0.1	1	0.1	65.12669259	0.00061947
							(62.79495922)	(0.00064863)
10							65.12922654	0.00062917
							(62.79758110)	(0.00065904)
15							65.12753724	0.00062270
							(62.79583318)	(0.00065210)
	5						1471.47762556	0.00068543
							(1426.54669853)	(0.00071379)
	10						5856.94837366	0.00068882
							(5681.30677889)	(0.00071692)
		0.3					27.73265899	0.00066302
							(26.78147532)	(0.00070221)
		0.5					23.17614129	0.00059674
							(22.40607838)	(0.00063192)
			0.3				65.32082417	0.00136062
							(62.98748118)	(0.00141077)
			0.5				65.51495575	0.00209738
							(63.18000314)	(0.00216827)
				0.3			65.19500571	0.00088078
							(62.86163437)	(0.00091310)
				0.5			65.24510200	0.00107206
							(62.91052949)	(0.00110670)
					3		196.05103681	0.00018729
							(189.22424073)	(0.00019863)
					5		328.33796393	0.00010385
							(317.24410090)	(0.00011074)
						0.3	78.74674918	0.00051393
							(76.17793939)	(0.00053647)
						0.5	92.08469965	0.00044049
							(89.24187178)	(0.00045906)

5. Final Remarks

Casson hybrid nanofluid flow for the entropy creation and the pre-exponential factor law in Darcy Forchheimer medium over a thin needle is examined. The numerical results are obtained for different dimensionless constraints and discussed in detail with the help of plots. The major outcomes of the present study are as follows:

1. Axial velocity decreases with augmentation of porosity parameter, Darcy parameter but reverse trend is seen in case of needle size.

2. Thermal distribution enhances with escalating values of Brinkman number and size of the needle while it declines for porosity, Darcy parameter and Prandtl number.

3. The rise in the values of Darcy, thermophoresis, Brinkman number, Activation energy parameter enhances the concentration.

4. Schmidt number and length ratio parameter decreases the concentration profile.

5. Surface drag force increases with heightening values of porosity parameter.

6. Brinkman number and porosity parameters will elevate the entropy generation.

7. Bejan number decreases for escalating values F_r but opposite trend is observed in porosity parameter.

8. Hybrid nanofluid has a greater impact than nanofluid in velocity, thermal and concentration profiles.

Acknowledgement

The authors extend their appreciation to the Deanship of Scientific Research at King Khalid University, Abha 61413, Saudi Arabia for funding this work through research groups program under grant number R.G.P-1/88/42.

References

[1] S.U.S. Choi, Argonne, IL (United States), 1995.
[2] M. I. Khan and F. Alzahrani, Mathematical Methods in the Applied Sciences **44**, 7766 (2021).
[3] A. Alhadhrami, H. A. H. Alzahrani, R. Naveen Kumar, R.J. Punith Gowda, K. Sarada, B. M. Prasanna, J. K. Madhukesh, and N. Madhukeshwara, Case Studies in Thermal Engineering **28**, 101404 (2021).
[4] V. Kumar, J. K. Madhukesh, A. M. Jyothi, B. C. Prasannakumara, M. Ijaz Khan, and Y.-M. Chu, Computational and Theoretical Chemistry **1200**, 113223 (2021).
[5] S. Ahmad, S. Nadeem, and M. N. Khan, Physica Scripta, **96**, 075205 (2021).
[6] Y.-M. Chu, H. M. A. Javed, M. Awais, M. I. Khan, S. Shafqat, F. S. Khan, M. S. Mustafa, D. Ahmed, S. U. Khan, and R. M. A. Khalil, Catalysts **11**, 54 (2021).
[7] J. K. Madhukesh, R. Naveen Kumar, R. J. Punith Gowda, B. C. Prasannakumara, G. K. Ramesh, M. Ijaz Khan, S. Ullah Khan, and Y.-M. Chu, Journal of Molecular Liquids **335**, 116103 (2021).
[8] S. Farooq, M. Ijaz Khan, M. Waqas, T. Hayat, and A. Alsaedi, Computer Methods and Programs in Biomedicine **184**, 105086 (2020).
[9] R. J. P. Gowda, R. Naveenkumar, J. K. Madhukesh, B. C. Prasannakumara, and R. S. R. Gorla, Proceedings of the Institution of Mechanical Engineers, Part N: Journal of Nanomaterials, Nanoengineering and Nanosystems 239779142098028 (2021).
[10] G. K. Ramesh, E. H. Aly, S. A. Shehzad, and F. M. Abbasi, Bödewadt flow and heat transfer of hybrid nanomaterial, International Journal of Ambient Energy, https://doi.org/10.1080/01430750.2020.1818127 (2021).
[11] S. Ahmad and S. Nadeem, Applied Nanoscience **10**, 5449 (2020).
[12] A. M. Jyothi, R. S. V. Kumar, J. K. Madhukesh, B. C. Prasannakumara, and G. K. Ramesh, Heat Transfer, https://doi.org/10.1002/htj.22221 (2021).
[13] W. Alghamdi, T. Gul, M. Nullah, A. Rehman, S. Nasir, A. Saeed, and E. Bonyah, AIP Advances **11**, 015016 (2021).
[14] J. Madhukesh, A. Alhadhrami, R. Naveen Kumar, R. Punith Gowda, B. Prasannakumara, and R. Varun Kumar, Proceedings of the Institution of Mechanical Engineers, Part E: Journal of Process Mechanical Engineering, 09544089211039305 (2021).
[15] N. I. Kamis, M. F. M. Basir, S. Shafie, T. K. A. Khairuddin, and L. Y. Jiann, IOP Conf. Ser.: Mater. Sci. Eng. **1078**, 012019 (2021).
[16] S. N. A. Salleh, N. Bachok, N. M. Arifin, and F. M. Ali, CFD Letters **12**, 22 (2020).
[17] R. N. Kumar, R. J. P. Gowda, J. K. Madhukesh, B. C. Prasannakumara, and G. K. Ramesh, Physica Scripta **96**, 075210 (2021).
[18] I. Waini, A. Ishak, and I. Pop, Mathematics **8**, 612 (2020).
[19] I. Tlili, H. A. Nabwey, M. G. Reddy, N. Sandeep, and M. Pasupula, Ain Shams Engineering Journal **12**, 1025 (2021).
[20] Hashim, A. Hamid, and M. Khan, Chinese Journal of Physics **64**, 227 (2020).
[21] H. Darcy, Victor Dalmont, 1856.
[22] P. Forchheimer, Zeitschrift des Vereins deutscher Ingenieure, Düsseldorf. (1901).
[23] M. Ijaz Khan, S. Qayyum, F. Shah, R. Naveen Kumar, R. J. Punith Gowda, B. C. Prasannakumara, Y.-M. Chu, and S. Kadry, Ain Shams Engineering Journal, https://doi.org/10.1016/j.asej.2021.01.028 (2021).
[24] P.-Y. Xiong, A. Hamid, Y.-M. Chu, M. I. Khan, R. J. P. Gowda, R. N. Kumar, B. C. Prasannakumara, and S. Qayyum, European Physical Journal Plus **136**, 315 (2021).
[25] G. K. Ramesh, S. A. Shehzad, and M. Izadi, Arabian Journal of Science and Engineering **45**, 9569 (2020).
[26] J. Buongiorno, Journal of Heat Transfer **128**, 240 (2006).
[27] P. Rana, N. Srikantha, T. Muhammad, and G. Gupta, Case Studies in Thermal Engineering **27**, 101340 (2021).
[28] M. Ijaz, M. Ayub, M. Y. Malik, H. Khan, A. A. Alderremy, and S. Aly, Physica Scripta **95**, 025402 (2020).
[29] M. Turkyilmazoglu, European Physical Journal Plus **136**, 376 (2021).
[30] A. Aziz, W. Jamshed, Y. Ali, and M. Shams, Discrete &

Continuous Dynamical Systems-S **13**, 2667 (2020).
[31] N. S. Wahid, M. E. H. Hafidzuddin, N. M. Arifin, M. Turkyilmazoglu, N. A. A. Rahmin, CFD Letters **12**, 1 (2020).
[32] P. Sreedevi, P. Sudarsana Reddy, and A. Chamkha, SN Applied Sciences **2**, 1222 (2020).
[33] J. K. Madhukesh, G. K. Ramesh, B. C. Prasannakumara, S. A. Shehzad, and F. M. Abbasi, Applied Mathematics and Mechanics (English Edition) **42**, 1191 (2021).
[34] T. Hayat, M. Khan, M. I. Khan, A. Alsaedi, and A. Ayub, Plos One **12**, e0180976 (2017).
[35] E. Azhar, Z. Iqbal, S. Ijaz, and E. N Maraj, Pramana **91**, 61 (2018).
[36] M. I. Khan, S. Qayyum, T. Hayat, M. I. Khan, and A. Alsaedi, International Journal of Heat and Mass Transfer, **133**, 959 (2019).
[37] Z. Iqbal, E. Azhar, and E. N. Maraj, Chaos, Solitons & Fractals **114**, 312 (2018).
[38] M. I. Khan, A. Alsaedi, T. Hayat, and N. B. Khan, Computer Methods and Programs in Biomedicine **179**, 104973 (2019).
[39] E. N. Maraj, S. Shaiq, and Z. Iqbal, Journal of Molecular Liquids **262**, 275 (2018).
[40] M. Waqas, M. I. Khan, T. Hayat, M. M. Gulzar, and A. Alsaedi, Chaos, Solitons & Fractals **130**, 109415 (2020).
[41] R. Mehmood, S. Rana, and E. N. Maraj, Communications in Theoretical Physics **70**, 106 (2018).
[42] T. Hayat, M. I. Khan, M. Tamoor, M. Waqas, and A. Alsaedi, Results in Physics **7**, 1824 (2017).
[43] E. N. Maraj, Z. Iqbal, and S. Shaiq, International Journal of Hydrogen Energy **43**, 10915 (2018).